Ptychographic X-ray computed tomography analysis of cement pastes

MIGUEL ARANDA[1,2,a], Ana Cuesta[1,b], Angeles De la Torre [1,c], Pavel Trtik[3,d], Ana Diaz[3,e]

[1]Departamento de Química Inorgánica, Cristalografía y Mineralogía, University of Malaga and ALBA synchrotron, Málaga, Spain
[2]ALBA SYNCHROTRON, Barcelona, Spain
[3]Paul Scherrer Institut, Villigen, Switzerland

[a]g_aranda@uma.es
[b]acuesta@cells.es
[c]mgd@uma.es
[d]pavel.trtik@psi.ch
[e]ana.diaz@psi.ch

ABSTRACT

Ptychographic X-ray computed tomography provides 3D electron mass density and attenuation coefficient distributions of unaltered cement pastes with an isotropic resolution below 100 nm. This imaging technique allows quantitatively distinguishing between different components with very similar absorption contrast.

Samples were measured at the cSAXS beamline: i) a neat Portland Cement (PC); ii) a PC-CC blend: 80 wt% of PC and 20 wt% of CaCO3, and iii) a PC-FA blend: 70 wt% of PC and 30 wt% of fly ash. The main aim of this study is to have a better insight of the microstructure of the amorphous/nanocrystalline gels with submicrometer spatial resolution. It is worth noting that it is possible to determine the gel mass density and water content within the attained 3D resolution (about 100 nm).

Here, we focused on the spatial distribution of the different components and in the variation of the electron density values which are very related to the mass density values. Special attention is paid to the density values of the amorphous (or nanocrystalline) components. The electron and mass density values of the C-S-H gel for three pastes are thoroughly analyzed. The density values range from 2.05-2.10 g·cm-3 for high density C-S-H gel for neat PC and PC-CC pastes to 1.80 g.cm-3 for low density C-S-H gel in PC-FA paste. The density value of poorly crystalline iron-siliceous hydrogarnet component, d=2.52 g·cm-3, has also been determined.
A summary of our ongoing research focused on the analyses of cement pastes by synchrotron PXCT is reported and discussed

Ptychographic X-ray computed tomography analysis of cement pastes

Miguel A. G. Aranda[1,2,a], Ana Cuesta[1,b], Angeles De la Torre[1,c], Pavel Trtik[3,4,d], Ana Diaz[3,e]

[1] *Departamento de Química Inorgánica, Cristalografía y Mineralogía, University of Malaga, Spain*
[2] *ALBA Synchrotron, Carrer de la Llum 2-26, E-08290 Cerdanyola del Vallès, Barcelona, Spain*
[3] *Paul Scherrer Institut, 5232 Villigen PSI, Switzerland*
[4] *Faculty of Civil Engineering, Czech Technical University in Prague, 166 29 Prague, Czech Republic*

[a]g_aranda@uma.es
[b]acuesta@cells.es
[c]mgd@uma.es
[d]pavel.trtik@psi.ch
[e]ana.diaz@psi.ch

1. INTRODUCTION

Cement pastes have a large number of component phases and the knowledge of the mass densities are key to understand volume stabilities and to relate weight fractions to volumes fractions. Mass densities for crystalline materials are well determined (Balonis & Glasser, 2009). However, mass densities of amorphous (or nanocrystalline) components are much more difficult to establish with contradicting reports. For instance, an striking high mass density value, 2.44 gcm^{-3}, has been used for micrometer-sized calcium silicate hydrate (C-S-H) gel (Deboodt et al., 2019) which should result in wrong volume-content analyses. Ptychographic X-ray computed tomography (PXCT) allows a non-invasive assessment of electron (and mass) density at the meso and microscales (Diaz et al., 2012).

PXCT is a non-destructive scanning imaging technique which uses the coherence properties of synchrotron radiation (Dierolf et al., 2010). PXCT replaces the post-sample X-ray optics by phase retrieval algorithms which, combined with the ptychographic approach, make the technique very reliable and robust (Faulkner & Rodenburg, 2004; Rodenburg et al., 2007). This technique allows quantitatively distinguishing between different components with very similar absorption contrast, which is not possible with standard (absorption-based) synchrotron X-ray tomography. Moreover, PXCT (Dierolf et al., 2010) combines ptychography and tomography to simultaneously provide two 3D volumes of the difference from one of the real part of the refractive index, $\delta(\mathbf{r})$, and the imaginary part of the refractive index, $\beta(\mathbf{r})$. Consequently, the complete complex-valued refractive index of the sample can be obtained (da Silva et al., 2015) as follows:

$$n(\mathbf{r})=1-\delta(\mathbf{r})+i\beta(\mathbf{r}) \quad (1)$$

The 3D electron density distribution, $n_e(r)$, can also be estimated using equation (2) (Diaz et al., 2012)

$$n_e(\boldsymbol{r}) = \frac{2\pi\delta(\boldsymbol{r})}{r_0\lambda^2} \quad (2)$$

where r_0 is the classical electron radius and λ is the X-ray wavelength. Finally, if the chemical composition is known (Diaz et al., 2012), the mass density can be estimated according to equation (3)

$$\rho(\boldsymbol{r}) = \frac{n_e(\boldsymbol{r})A}{N_A Z} \quad (3)$$

where N_A is Avogadro's number, A is the molar mass, and Z is the total number of electrons in the formula unit.

PXCT can also provide 3D electron mass density and attenuation coefficient distributions of cement pastes as it was already reported in previous publications (Trtik et al., 2013; da Silva et al., 2015; Cuesta et al., 2017; Cuesta et al., 2019) with an isotropic resolution close to 100 nm or better. PXCT was applied to investigate the hydration of a Portland Cement (PC). The composition, density and microstructure of their components were analysed (Trtik et al., 2013). Furthermore, the 3D tomograms

were segmented and the mass densities of the different phases were quantitatively determined. However, this sample was slightly altered because it was impregnated with an epoxy resin for the PXCT study.

This technique has also been used to image the hydration of alite without sample treatment. In this case, the densities and water contents of C-S-H gels were determined (da Silva et al., 2015). Another recent use of PXCT in cements has been the study of aluminium hydroxide gels in ye'elimite-containing pastes (Cuesta et al., 2017a; Cuesta et al., 2017b). The main outcome of these studies was the mass density measurements of nano-gibbsite gels. In our previous work (Cuesta et al., 2017a), it was reported the composition and mass density of two aluminium hydroxide gel agglomerates: $(CaO)_{0.04}Al(OH)_3 \cdot 2.3H_2O$ with 1.48(3) $g \cdot cm^{-3}$ and $(CaO)_{0.12}Al(OH)_3$ with 2.05(3) $g \cdot cm^{-3}$. The calcium contents within the aluminium hydroxide gel agglomerates likely came from the very fine intermixing of nano-gibbsite with $Ca_3Al_2(OH)_{12}$ and other calcium aluminate hydrates (Cuesta et al., 2017a). Moreover, an *in-situ* PXCT study of this paste was performed in order to characterize the evolution of the dissolution of selected anhydrous ye'elimite particles with time (Cuesta et al., 2017b).

Finally, and very recently, PXCT was also employed (Cuesta et al., 2019) for obtaining spatially-resolved information on three unaltered PC cement samples at 5 months of hydration: Portland paste, Portland-calcite paste and Portland-fly ash paste. In that work, the combined use of electron density and absorption tomograms was used for identifying components with quite similar electron densities but different attenuation coefficients and chiefly in the segmentation procedure for obtaining accurate analyses for these complex mixtures, for instance C-S-H gel and crystalline $Ca(OH)_2$. The chemical composition and mass density of the precipitated C-S-H gel was also determined. All the electron and mass densities were experimentally determined for each phase including the Fe–Al siliceous hydrogarnet gel. Moreover, the segmentation study allowed separating and quantifying the different phases of each paste. An important result obtained in this work (Cuesta et al., 2019) was that the smaller reaction degree for the Portland cement – calcite (PC-CC) blend paste allowed to distinguish the inner product and outer product of C-S-H gel. Finally, for the Portland cement – Fly Ash (PC-FA) blend paste, the measured FA reaction degree was also determined to be close to 30%.

This publication deals with the PXCT data for PC, PC-CC and PC-FA already analysed and reported (Cuesta et al., 2019). Here, the attenuation tomograms neither with the segmentation procedures and results are dealt with. This paper focused on a thorough analysis of the electron density profiles (very much related to the mass densities) across selected particles/regions/volumes. A deep characterization of the electron density spatial arrangement is carried out for a better microstructural description of these Portland pastes.

2. MATERIALS AND METHODS

2.1 Sample preparation

For this work, the following anhydrous samples were used: a commercial PC from FYM S.A. (Málaga, Spain), Fly ash Class F obtained from power station of Lada (Spain) (García-Maté et al., 2013) and $CaCO_3$ from sigma Aldrich with a purity of 99.0%. Then, three pastes were used for performing the PXCT studies. The preparation of these pastes has been already described (Cuesta et al., 2019) and it is summarized here:

a) The commercial PC.

b) The PC-CC blend: a mixture of 80 wt% of PC and 20 wt% of $CaCO_3$.

c) The PC-FA blend: a mixture of 70 wt% of PC and 30 wt% of FA.

Firstly, after milling all the samples, they were loaded inside capillaries using an ultrasound bath to help the powder to reach the tip. Secondly, the capillary was filled up with distilled water and both ends of the capillary were sealed with special UV-hardening glue. The prepared pastes were placed at room temperature for 5 months of hydration and finally they were measured at the cSAXS beamline, at the Swiss Light Source, Paul Scherrer Institute (Villigen, Switzerland).

2.2 PXCT experiment and data processing

The three prepared pastes were measured at the cSAXS beamline at the Swiss Light Source, Paul Scherrer Institute (Villigen, Switzerland) using an instrument described elsewhere (Holler et al., 2014) which uses laser interferometry for accurate positioning of the specimen with respect to the beam-defining optics (Holler & Raabe, 2015). The photon energy was 6.2 keV. Diffraction patterns were collected with an Eiger 500k detector placed 7.305 m downstream of the sample satisfying the ptychography sampling conditions (da Silva & Menzel, 2015; Edo et al., 2013). From the experimental conditions, the resulting pixel size in the reconstructed images was 38.95 nm. A total of 800 projections within the 0-180º angular range were acquired for the PC paste and 1300 for PC-FA and PC-CC pastes. The total acquisition time for all diffraction patterns was between 17 and 22 h. This time also included the time necessary for sample motion. Additional experimental details about the measurements can be found elsewhere (Cuesta et al., 2019).

Ptychographic reconstructions were carried out with a few hundred iterations of a difference map algorithm (Thibault et al., 2009) followed by a few hundred iterations of a maximum likelihood optimization used as a refinement (Thibault & Guizar-Sicairos, 2012). The spatial resolution of the tomograms was determined by Fourier Shell Correlation (FSC) with a threshold based on the half-bit criterion (Holler et al., 2014; van Heel & Schatz, 2005) and the results were 80, 56 and 59 nm for neat PC, PC-CC and PC-FA blends, respectively. Additional details about the tomographic reconstructions (Guizar-Sicairos et al., 2011) of the samples can be found in the previous paper (Cuesta et al., 2019).

3. RESULTS AND DISCUSSION

The water-to-cement (w/c) and water-to-binder (w/b) mass ratios of the scanned parts of the capillaries were determined as previously described (Cuesta et al., 2019). Here, it is just summarize the final results for easy reference. For the neat PC paste, the w/c ratio was 0.27. For the PC-CC blend paste, the w/c and w/b ratios were 0.33 and 0.27, respectively. For the PC-FA blend paste, the w/c and w/b ratios were 0.43 and 0.30, respectively.

Table 1 reports the chemical formula for all the material phases that were found in the three samples and the corresponding numerical labels used in the figures and the abbreviations used in the text. Moreover, the average electron and mass densities determined for each phase (Cuesta et al., 2019) are also reported in Table 1.

Table 1. Chemical formula of the phases including abbreviation and the phase number used in the figures. The electron and mass density values are also included (Cuesta et al., 2019).*

Phase number	Phase abbreviation	Chemical formula	Determined electron den. ($e^-·Å^{-3}$)	Theoretical electron den. ($e^-·Å^{-3}$)	Determined mass density ($g·cm^{-3}$)	Crystallogr. mass density ($g·cm^{-3}$)
1	AFt	$Ca_6Al_2(SO_4)_3(OH)_{12}·26H_2O$	0.57(1)	0.56	1.80(1)	1.78
2	LD_C-S-H	$\sim(CaO)_{1.8}(SiO_2)(H_2O)_6$	0.56(2)	-	~1.77	-
3	HD_C-S-H	$\sim(CaO)_{1.8}(SiO_2)(H_2O)_4$	0.65(1)	-	~2.10	-
4	CH	$Ca(OH)_2$	0.69(1)	0.69	2.23(2)	2.23
5	Fe-Al-Si-**Hg**	$\sim Ca_3FeAl(SiO_4)_{0.84}(OH)_{8.64}$	0.77(1)	-	~2.50	-
6	FA	$\sim SiO_2$	0.77(2)	-	~2.55	-
7	CC	$CaCO_3$	0.83(1)	0.82	2.75(1)	2.71
8	C_3S	Ca_3SiO_5	0.96(1)	0.95	3.20(1)	3.15
9	C_2S	Ca_2SiO_4	1.00(1)	0.99	3.32(3)	3.30
10	MgO	MgO	1.07(1)	1.07	3.52(5)	3.58
11	C_4AF	Ca_2AlFeO_5	1.07(1)	1.10	3.60(5)	3.73

* In this manuscript, hydrated component phases are depicted in orange and anhydrous phases in blue.

3.1 PC paste

The PC sample was hydrated for 5 months at RT. After that time, the PXCT study determined that this paste contained eight different phases, see Figure 1a. The electron density values for each component were extracted from the electron density histogram and these data are given in Table 1. These electron density values are averaged within the resolution volume ~100×100×100 nm^3. On the one hand, the sample contained four unreacted phases, C_3S, C_2S, C_4AF and MgO that are labelled with blue numbers in Figure 1a. On the other hand, the hydrated phases found for this sample were AFt, portlandite, high-density HD_C-S-H gel and iron-siliceous hydrogarnet, labelled with orange

numbers in Figure 1a.

In order to perform a deep study about the structural characterization of the PC pastes, the electron densities profiles of different particles of the main phases were measured. This characterization was carried out with ImageJ/Fiji shareware (Abràmoff et al., 2004; Schindelin et al., 2012). It is important to highlight that the horizontal (blue or orange) lines in Figure 2 show the average values of the electron densities obtained for the component phases using ten different volumes/particles (Cuesta et al., 2019) which are reported in Table 1.

Figure 2a shows a dicalcium silicate particle with some fractures/defects. The electron density along this C_2S particle matches very well with the determined average value, 1.00 $e^{-}\cdot Å^{-3}$ (0.99 $e^{-}\cdot Å^{-3}$ is the expected value from the crystal structure) and the profile is very regular. Moreover, the electron density inside the small fracture is very close to that electron density determined for high density C-S-H gel, 0.65 $e^{-}\cdot Å^{-3}$, showing the good resolution of the PXCT data and that the hydration process advances along the defects if they are connected to the surface of the particle (see Figure 2a). Figure 2b shows another unreacted set of particles which is composed of C_2S and MgO/C_4AF. These two phases cannot be easily distinguished because their electron densities are very similar, their experimental values were determined to be close to 1.07 $e^{-}\cdot Å^{-3}$. The volume showed in Figure 2b, and also in Figure 2e, presents an additional (high density) phase which is surrounding the anhydrous particles. This additional phase has an electron density close to 0.77 $e^{-}\cdot Å^{-3}$, which was assigned to a poorly crystalline Fe–Al siliceous hydrogarnet (Cuesta el al., 2019). Figure 2f shows the electron density profile of this component, Fe-Al-Si-**Hg**, along a selected region. Moreover, this poorly crystalline phase is usually found surrounding unreacted C_4AF and it has a mass density of ~2.50 $g\cdot cm^{-3}$. The electron density profile is not very homogenous along the particle likely due to the poor crystallinity of this Fe-Al-Si-**Hg** phase**.** Figure 2c shows a tricalcium silicate particle with a uniform density across the particle, close to 0.96 $e^{-}\cdot Å^{-3}$ (0.95 $e^{-}\cdot Å^{-3}$ is expected from the crystal structure). In addition, the C-S-H gel surrounding the C_3S particle presents a homogenous electron density close to the average value, 0.65 $e^{-}\cdot Å^{-3}$. Figure 2d shows a region of crystalline portlandite in order to highlight the homogeneity of the electron density of this component along the entire measured region and the agreement with the expected value from its crystal structure, see Table 1. Finally, Figures 2g, 2h and 2i show three different regions randomly selected for the C-S-H gel in this PC paste. The electron density profiles measured along the different regions show that the C-S-H gel presents here a high degree of homogeneity and the electron density value is quite constant, 0.65 $e^{-}\cdot Å^{-3}$, which means that the water content is also fairly constant, $(CaO)_{1.80}SiO_2(H_2O)_{4.0}$, as determined in the previous publication (Cuesta et al., 2019). The density of this gel was determined to be ~2.10 $g\cdot cm^{-3}$. Finally, it is important to highlight that Figure 2i was selected also to show some small particles of AFt which are intermixed with the gel. It can be observed that the density of AFt is quite close to its average determined value, 0.57 $e^{-}\cdot Å^{-3}$ (0.56 $e^{-}\cdot Å^{-3}$ is expected from the crystal structure), which means that the resolution of this PXCT data is very good and the partial volume effect is negligible here.

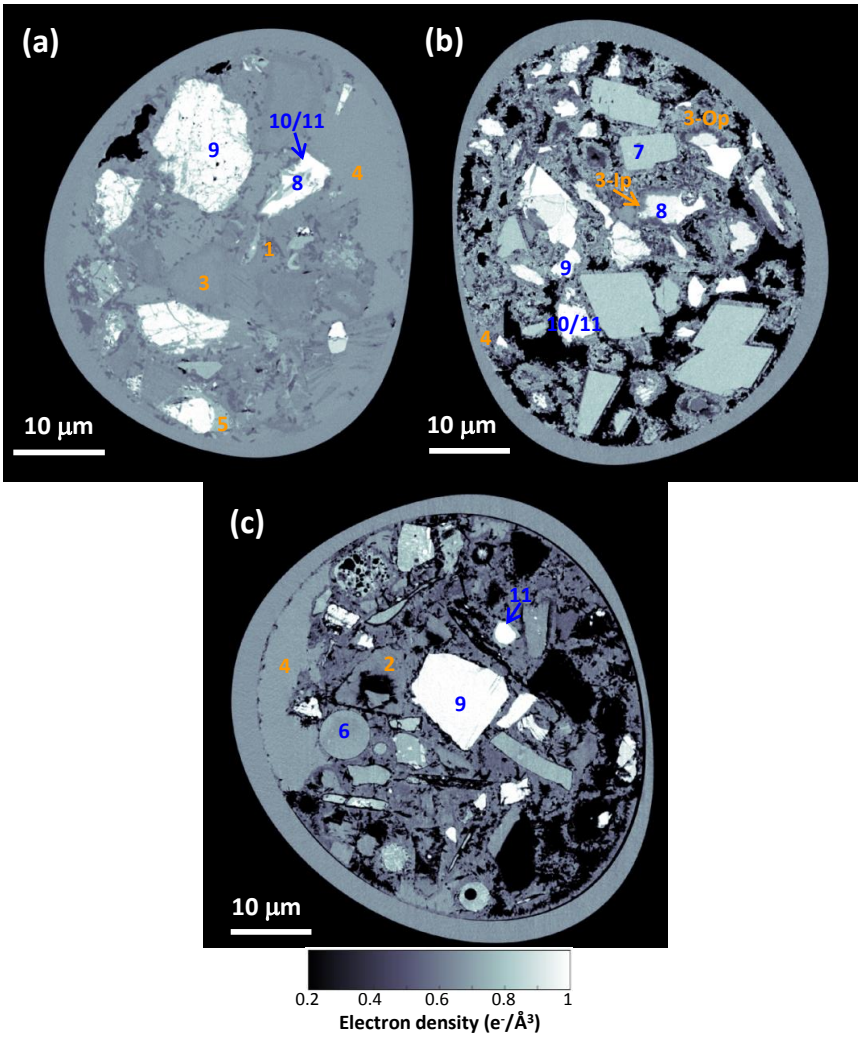

Figure 1. Selected slices of the PXCT electron density tomograms for (a) PC paste, (b) PC-CC paste and (c) PC-FA paste, after 5 months of hydration at room temperature.

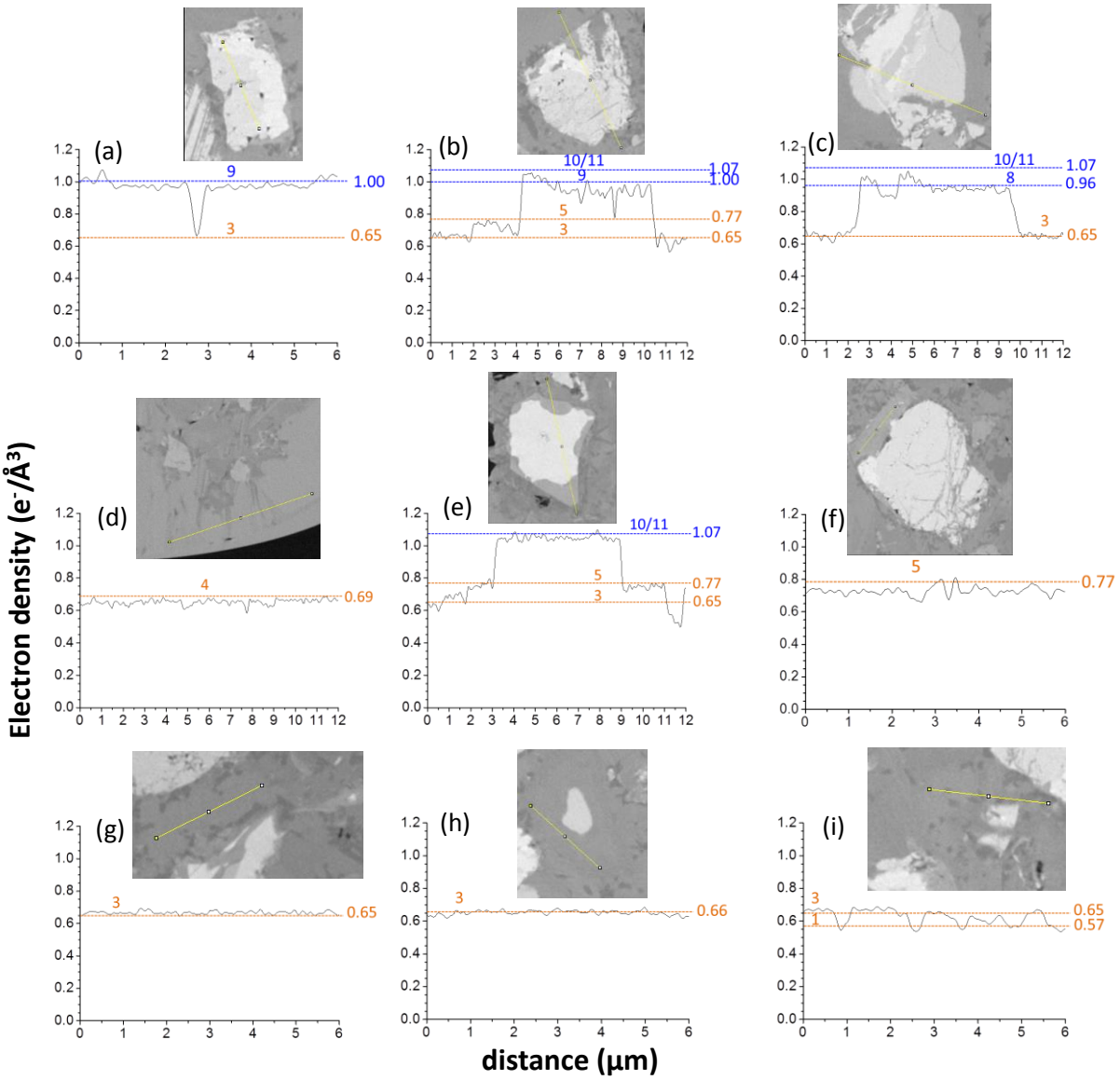

Figure 2. Nine selected regions in the electron density tomogram of the PC paste highlighting different component phases. Selected lines (yellow) are drawn to show the variation of the electron density values along the particles/regions (discontinuous black lines). Horizontal blue lines show the average values of the electron densities obtained for the anhydrous phases and the orange lines are used for the hydrated component phases (Cuesta et al., 2019). Electron density values taken from Table 1 using ten different particles.

3.2 PC-CC paste

The PC-CC sample was also hydrated for 5 months. After that time, the PXCT study determined that this paste contained eight component phases, see Figure 1b. The electron density values for each phase were extracted from the electron density histogram as reported in Cuesta et al. (2019) and they are summarized in Table 1. The sample contained five anhydrous (unreacted) phases C_3S, C_2S, C_4AF, MgO and $CaCO_3$, labelled with blue numbers in Figure 1b (see Table 1). On the other hand, the hydrated phases that could be properly distinguished for this sample were portlandite and HD_C-S-H gel, indicated by orange numbers in Figure 1b. Moreover, a third hydrated phase was found and it was identified as a mixture of phases such as AFt, AFm-type phases intermixed with additional water, average electron density close to 0.45 $e^{-}\cdot Å^{-3}$.

The microstructure and electron density of the main components of this PC-CC paste have been studied by using the electron density profiles of selected volumes/regions/particles. Firstly, Figure 3a and 3b show two different $CaCO_3$ particles which present a constant electron density profile across the

different particles and very close to its determined average value, 0.83 $e^{-}\cdot Å^{-3}$ (0.82 $e^{-}\cdot Å^{-3}$ is expected from the crystal structure). The morphologies of these particles are very well defined with sharp edges. Furthermore, it can be observed that a very thin layer of hydrates (lower density component) is deposited on the surfaces of the $CaCO_3$ particles. Secondly, Figure 3c shows a C_3S particle surrounded by C-S-H gel. The electron density profile for the anhydrous particle matches quite well with the average C_3S value, 0.96 $e^{-}\cdot Å^{-3}$, in full agreement with the results for the previous pastes, see Fig. 2c. Figure 3f shows the same particle as Figure 3c but in this case, the electron density is displayed along the C-S-H gel. Moreover, as it has been previously reported (Cuesta et al., 2019), two different C-S-H gels could be distinguished for the OPC-CC paste, the inner and the outer products. It was determined that the electron density of the C-S-H gel that precipitated within the boundaries of the pristine C_3S particles, inner product (Ip-C-S-H), has lower electron density than that precipitated in the capillary pore regions, outer product (Op-C-S-H). In this case, the gel surrounding the fraction of unreacted C_3S particles in Figures 3f and 3g is identified as Ip-C-S-H gel. It can be seen that its electron density values are variable and normally slightly lower than the average value for the C-S-H gel in this sample, 0.65 $e^{-}\cdot Å^{-3}$. It was reported (Cuesta et al., 2019) that the degree of variation of the electron density in the inner product of the C-S-H can be as large as 25% with a minimum value of 0.53 $e^{-}\cdot Å^{-3}$. On the other hand Figures 3h and 3i show two different regions of the Op-C-S-H gel. It can be observed that the electron density of the outer product of C-S-H gel is on average 0.65 $e^{-}\cdot Å^{-3}$ although this phase also presents a high degree of heterogeneity in comparison to the C-S-H gel found in the PC paste, likely due to the presence of intermixing with some other minor phases (monocarbonate, hemicarbonate, ettringite, etc.). Finally, Figures 3c and 3d show two large regions of crystalline portlandite. The electron density along the selected line is quite homogenous and close to expected value, 0.69 $e^{-}\cdot Å^{-3}$, so no further discussion is required.

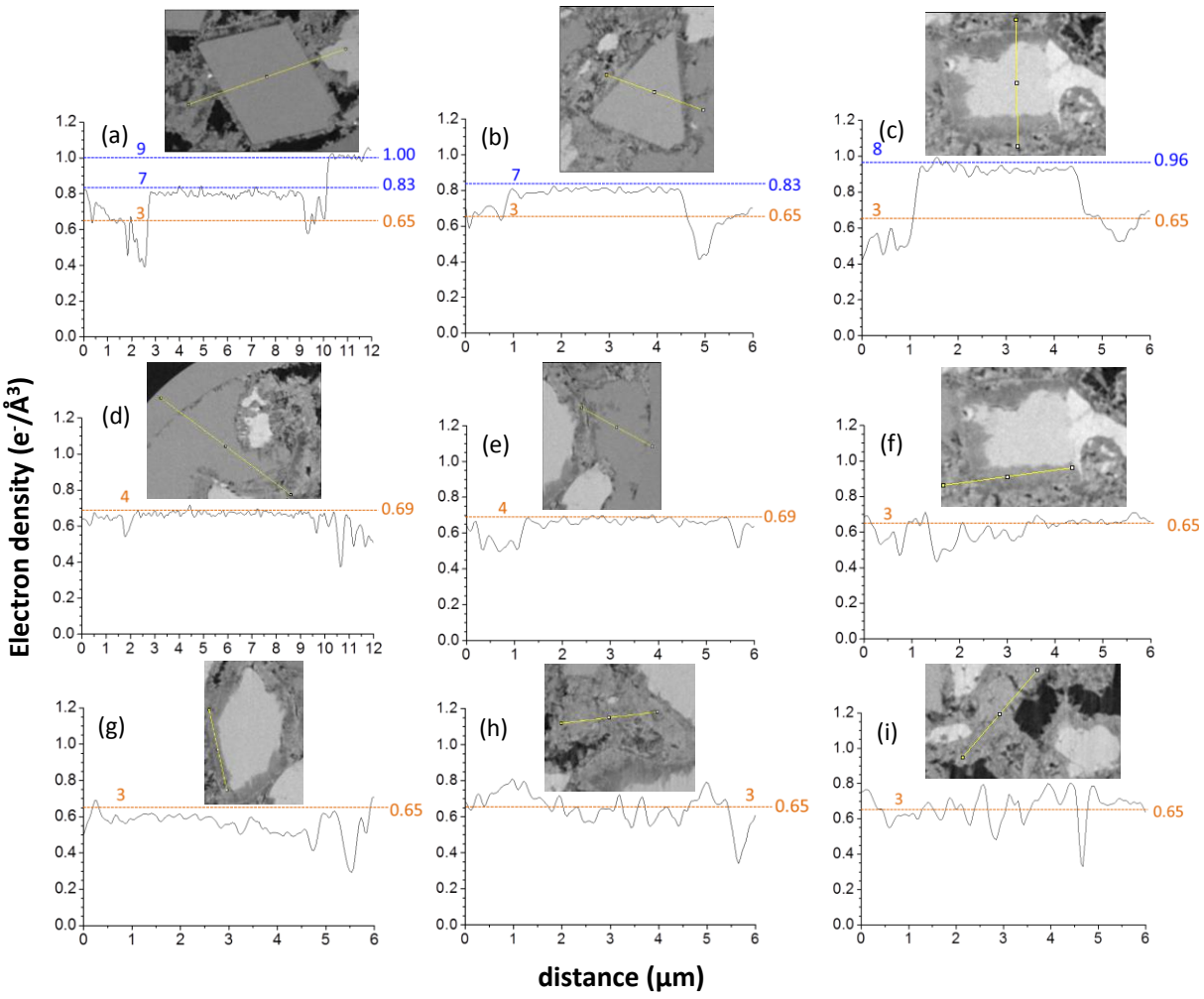

Figure 3. Nine selected regions in the electron density tomogram of the PC-CC paste highlighting different component phases. Details of the plots as in Figure 2.

3.3 PC-FA paste

After 5 months of hydration, it was determined by PXCT that the PC-FA paste contained six component phases (Cuesta et al., 2019). The anhydrous phases observed here were C_2S, MgO and FA as it is shown in Figure 1c. On the other hand, the hydrated component phases that could be properly distinguished for this paste were $Ca(OH)_2$ and LD_C-S-H gel (intermixed with AFt), see Figure 1c. The electron (and mass) densities of each phase are gathered in Table 1.

Figure 4 shows the regions that have been selected to perform a study about the microstructure of the PC-FA blend paste. Firstly, Figure 4a, 4b and 4c show three selected unreacted FA particles with regular spherical morphology. The size of the FA particles can vary between ~2 μm up to ~15 μm as shown in Figures 4a-c. The electron density across the FA particles is quite regular, being very close to the average value, 0.77 $e^{-}\cdot Å^{-3}$. Moreover, it can be observed that in all the FA particles there is some very small region of empty space surrounding the FA particles. For these and additional FA particles, the average size for the empty space was measured and it was determined to be close to 200 nm. The electron densities in these regions reached values close to that of water, n_e~0.33 $e^{-}\cdot Å^{-3}$, so it can be water porosity (see Figures 4a-c). However, it cannot be ruled out air porosity with the electron density values not reaching 0 due to the partial volume effect. These water/air filled spaces are likely due to shrinking during the hydration process because the relatively large w/c ratio of 0.43.

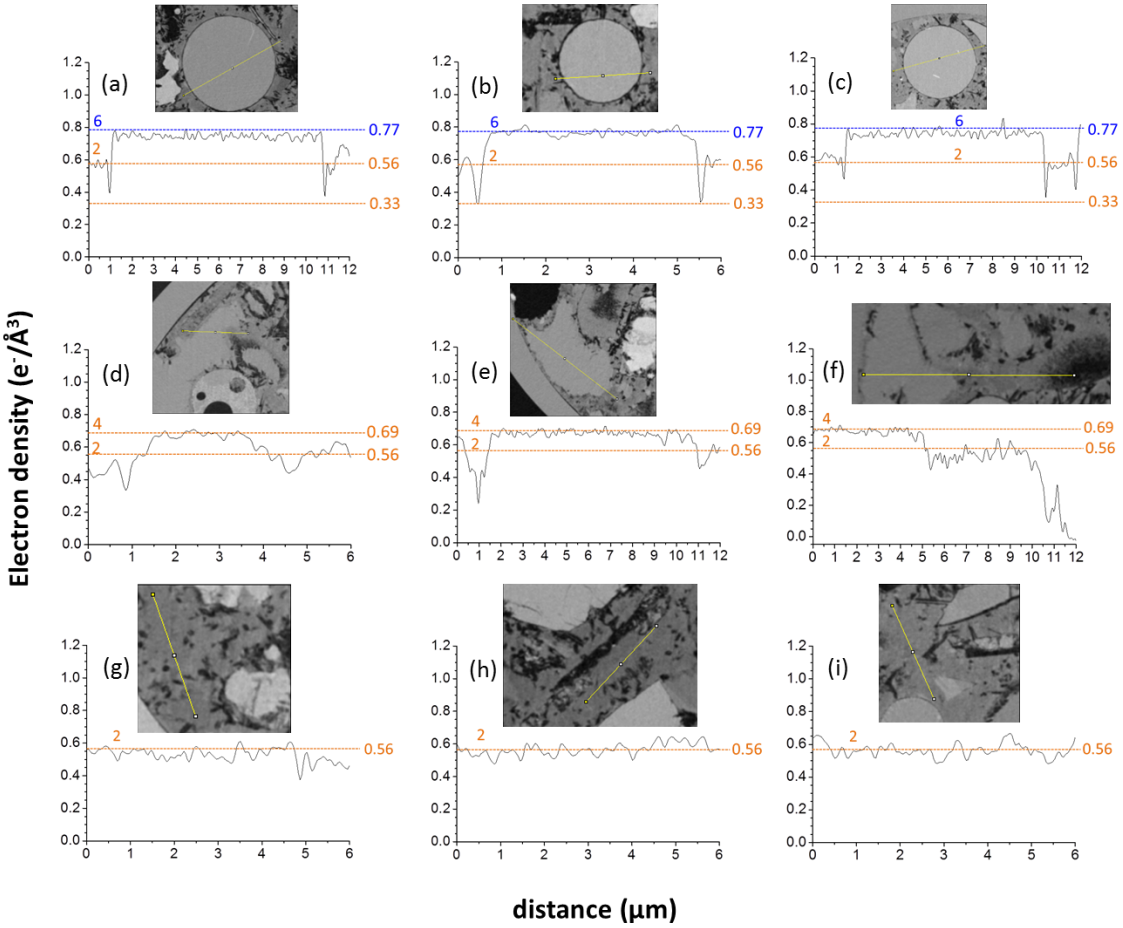

Figure 4. Nine selected regions in the electron density tomogram of the PC-FA paste highlighting different component phases. Details of the plots as in Figure 2.

Secondly, Figures 4d and 4e show two different regions of crystalline portlandite. As it was observed in the previous two pastes, the electron density value is quite constant, 0.69 $e^{-}\cdot Å^{-3}$. In addition, Figure 4f shows the electron density profile of a region with portlandite, C-S-H gel and an empty pore. The electron density of the C-S-H gel for this PC-FA paste was determined to be close to 0.56 $e^{-}\cdot Å^{-3}$. This electron density value corresponds to a low density gel, LD_C-S-H, which includes more pore water molecules, with a stoichiometry close to $(CaO)_{1.80}SiO_2(H_2O)_{6.0}$ (Cuesta et al., 2019). It is important to point out that the electron density of the region determined as LD_C-S-H gel can also contain some

amount of ettringite which cannot be separated of the C-S-H gel due to its similar electron density value, 0.57 $e^{-}\cdot Å^{-3}$. For this reason, the electron density profiles for the measured C-S-H gels are quite variable. Figure 4g, 4h and 4i show different selected regions of the C-S-H gel. It can be observed that the average value of the electron density of this region is around 0.56 $e^{-}\cdot Å^{-3}$. Moreover, it is also observed, see Figure 4f, that some small areas of the C-S-H gel are likely fine intermixed with water which makes the electron density profile more variable reaching values smaller than 0.57 $e^{-}\cdot Å^{-3}$.

Finally, it is worth noting that a low degree, ~30%, of pozzolanic reaction was indirectly observed three fold (Cuesta el at., 2019). I) the amount of $Ca(OH)_2$ determined through segmentation was smaller than that expected from the reaction degree of alite and belite. II) the amount of FA determined through segmentation was smaller than that weighted in the sample preparation step. III) and very importantly, plate-like empty volumes were observed, see Fig 1c and 4h. Moreover, in some case the empty volumes had sharp straight edges/faces. These regions cannot come from the consumption of water. It is hypothesized that the empty volumes with sharp straight surfaces originated from the reaction of crystalline portlandite when the paste is set. The dissolution of $Ca(OH)_2$, without precipitation to C-S-H, will cause these peculiar unconnected empty regions that we denominate 'air crystals' because of their flat surface. These 'air crystals' are the negative of the reacted (regular) portlandite particles. It is underlined that portlandite can crystallise in these pastes with hexagonal (regular) plate-like morphology but also with massive irregular shapes (Trtik et al., 2012).

4. GENERAL DISCUSSION AND CONCLUSIONS

For the neat PC paste with w/c=0.27, the average electron density for C-S-H gel was 0.66(1) $e^{-}/Å^3$. Assuming a Ca/Si ratio of 1.80, the mass density and water content compatible with this data is **ρ=2.10 gcm^{-3}** and $(CaO)_{1.8}SiO_2(H_2O)_{4.0}$. If an average Ca/Si ratio of 1.70 is assumed, PXCT data are compatible with **ρ=2.06 gcm^{-3}** and $(CaO)_{1.70}SiO_2(H_2O)_{3.7}$. It is underlined that the measured mass density of C-S-H gel is averaged over the micrometer scale with a spatial resolution close to 100nm. Therefore gel porosity is included but large capillary porosity is not. These density results for C-S-H gel are in agreement with several other reports (Cuesta et al., 2018; Muller et al., 2013; Jennings, 2008) but they are in total disagreement with a recently used value of 2.44 gcm^{-3} (Deboodt et al., 2019; Gastaldi et al., 2012) for imaging studies. The results of these two works should be revisited as the used density for C-S-H gel is not in line with state-of-the-art knowledge. Density values for the solid component of C-S-H gel (nanoglobules) range 2.50-2.60 gcm^{-3} (Thomas et al., 2010; Allen et al., 2007) but with an average composition of $(CaO)_{1.75}SiO_2(H_2O)_{1.8}$ (excluding gel porosity water content). These nanoglobules have sizes ~5nm that cannot be resolved with current 3D imaging techniques.

For neat PC, a high-density phase surrounding unreacted Ca_2AlFeO_5 was also found. The electron density of this hydrated phase was 0.77(2) $e^{-}/Å^3$, which for an assumed $Ca_3FeAl(SiO_4)_{0.84}(OH)_{8.64}$ stoichiometry, led to **ρ=2.52 gcm^{-3}** for this poorly crystalline iron-siliceous hydrogarnet component.

For the PC-calcite blend paste, w/c=0.33, the partial alite reaction degree has allowed to distinguish between inner product and outer product C-S-H gels. It is recalled that C-S-H gel growing in the volume formerly occupied by an alite particle is called inner-product, meanwhile C-S-H gel growing in the water pores or on other surfaces like calcite is termed outer-product. The density variations within inner product C-S-H were observed to be large, ranging 0.53-0.68 $e^{-}/Å^3$. The density variations within outer product C-S-H ranged 0.60-0.73 $e^{-}/Å^3$. Therefore, it is shown that inner product C-S-H cannot be directly related with higher density C-S-H. Furthermore, the average electron density value for C-S-H gel was found to be 0.64(1) $e^{-}/Å^3$. This value is compatible with a mass density of **ρ=2.05 gcm^{-3}** for this high-density C-S-H gel. It must also be highlighted that inner product C-S-H is firmly established as it surrounds unhydrated alite particles. However, outer product C-S-H is always a choice based on the surrounding environment as it cannot be totally ruled out a fully hydrated alite particle in that volume.

For the PC-FA blend paste, w/c=0.43, the average electron density for C-S-H gel is 0.56(1) $e^{-}/Å^3$. The mass density and water content compatible with this value is **ρ=1.80 gcm^{-3}** and $(CaO)_{1.8}SiO_2(H_2O)_{6.0}$ indicating a larger gel pore water content. Furthermore, empty spaces are found surrounding FA particles with a thickness close to 200 nm. We hypothesize that this effect is originated by the shrinking due to hydration. Finally, it is observed empty regions with flat surfaces are observed in these pastes that it was termed 'air crystals'. These (unconnected) regions could be the negative of the reacted (regular) portlandite particles due to the pozzolanic reaction in a set matrix.

5. ACKNOWLEDGEMENTS

This work has been done in collaboration with Isabel Santacruz and Mirko Holler, who have contributed to sample laboratory characterization and to the acquisition of the PXCT data, respectively. This work has been supported by Spanish MINECO through BIA2014-57658-C2-1-R and BIA2017-82391-R, which is co-funded by FEDER. We also thank Dr. Manuel Guizar-Sicairos for his valuable assistance with the ptychography and PXCT data analysis.

Data accessibility. All tomographic raw data underlying this article have be deposited on Zenodo at https://doi.org/10.5281/zenodo.2533863, to be used under the Creative Commons Attribution license.

6. REFERENCES

Abràmoff, MD, Magalhães, PJ, & Ram, SJ (2004). *Image Processing with ImageJ*. Biophotonics International, Volume 11, Issue 7, pp 36-42.

Allen, AJ, Thomas, JJ, & Jennings, HM (2007). *Composition and density of nanoscale calcium–silicate–hydrate in cement*. Nature Materials, Volume 6, Issue 4, pp 311-316.

Balonis, M, & Glasser, F (2009). *The Density of Cement Phases.* Cement and Concrete Research, Volume 39, Issue 9, pp 733-739

Cuesta, A, De la Torre, AG, Santacruz, I, Diaz, A, Trtik, P, Holler, M, Lothenbach, B, Aranda, MAG (2019). *Quantitative disentanglement of nanocrystalline phases in cement pastes by synchrotron ptychographic X-ray tomography.* IUCrJ. online

Cuesta, A, Zea-Garcia, JD, Londono-Zuluaga, D, De la Torre, AG, Santacruz, I, Vallcorba, O, Dapiaggi, M, Sanfélix, SG, Aranda, MAG (2018). *Multiscale understanding of tricalcium silicate hydration reactions.* Scientific Reports, 8, Article number:8544.

Cuesta, A, De la Torre, AG, Santacruz, I, Trtik, P, da Silva, JC, Diaz, A, Holler, M, Aranda, & MAG (2017a). *Chemistry and Mass Density of Aluminum Hydroxide Gel in Eco-Cements by Ptychographic X-ray Computed Tomography*. The Journal of Physical Chemistry C, Volume 121, Issue 5, pp 3044-3054.

Cuesta, A, De la Torre, AG, Santacruz, I, Trtik, P, Da Silva, JC, Diaz, A, Holler, M, & Aranda, MAG (2017b). *In situ hydration imaging study of a ye'elimite paste by ptychographic X-ray computed tomography*. En 39th International Conference on Cement Microscopy, ICMA 2017 (pp. 17-32).

da Silva, J. C., & Menzel, A. (2015). *Elementary signals in ptychography*. Optics express, Volume 23, Issue 26, pp 33812-33821.

da Silva, JC, Trtik, P, Diaz, A, Holler, M, Guizar-Sicairos, M, Raabe, J, Bunk, O, & Menzel, A (2015). *Mass Density and Water Content of Saturated Never-Dried Calcium Silicate Hydrates*. Langmuir, Volume 31, Issue 13, pp 3779-3783.

Deboodt, T, Wildenschild, D, Ideker, JH, & Isgor, OB (2019). *Use of iodine for improving phase quantification using x-ray tomography*. Cement and Concrete Research, Volume 116, pp 102-112.

Diaz, A, Trtik, P, Guizar-Sicairos, M, Menzel, A, Thibault, P, & Bunk, O (2012). *Quantitative x-ray phase nanotomography*. Physical Review B, Volume 85, Issue 2, 020104.

Dierolf, M, Menzel, A, Thibault, P, Schneider, P, Kewish, CM, Wepf, R, Bunk, O, & Pfeiffer, F (2010). *Ptychographic X-ray computed tomography at the nanoscale*. Nature, Volume 467, Issue 7314, pp 436-439.

Edo, TB, Batey, DJ, Maiden, AM, Rau, C, Wagner, U, Pešić, ZD, Waigh, TA, & Rodenburg, JM (2013). *Sampling in x-ray ptychography*. Physical Review A, Volume 87, Issue 5, pp 053850.

Faulkner, HML, & Rodenburg, JM (2004). *Movable Aperture Lensless Transmission Microscopy: A Novel Phase Retrieval Algorithm*. Physical Review Letters, Volume 93, Issue 2, pp 023903.

García-Maté, M, De La Torre, AG, León-Reina, L, Aranda, MAG, & Santacruz, I (2013). *Hydration studies of calcium sulfoaluminate cements blended with fly ash*. Cement and Concrete Research, Volume 54, pp 12-20.

Gastaldi, D, Canonico, F, Capelli, L, Boccaleri, E, Milanesio, M, Palin, L, Croce, G, Marone, F, Mader, K, & Stampanoni, M (2012). *In situ tomographic investigation on the early hydration behaviors of cementing systems*. Construction and Building Materials, Volume 29, pp 284-290.

Guizar-Sicairos, M, Diaz, A, Holler, M, Lucas, MS, Menzel, A, Wepf, RA, & Bunk, O (2011). *Phase tomography from x-ray coherent diffractive imaging projections*. Optics Express, Volume 19, Issue 22, pp 21345.

Holler, M, Diaz, A, Guizar-Sicairos, M, Karvinen, P, Färm, E, Härkönen, E., Ritala, M, Menzel, A, Raabe, J, & Bunk, O (2014). *X-ray ptychographic computed tomography at 16 nm isotropic 3D resolution*. Scientific Reports, Volume 4, Issue 1, pp 3857.

Holler, M, & Raabe, J (2015). *Error motion compensating tracking interferometer for the position measurement of objects with rotational degree of freedom*. Optical Engineering, Volume 54, Issue 5, pp 054101.

Jennings, HM(2008). *Refinements to colloid model of C-S-H in cement: CM-II*. Cement and Concrete Research, Volume 38, Issue3, pp 275-289.

Muller, ACA, Scrivener, KL, Gajewicz, AM, & McDonald, PJ (2013). *Densification of C–S–H Measured by ^{1}H NMR Relaxometry*. The Journal of Physical Chemistry C, Volume 117, Issue 1, pp 403-412.

Rodenburg, JM, Hurst, AC, Cullis, AG, Dobson, BR, Pfeiffer, F, Bunk, O, David, C, Jefimovs, K, & Johnson, I (2007). *Hard-X-Ray Lensless Imaging of Extended Objects*. Physical Review Letters, Volume 98, Issue 3, pp 034801.

Schindelin, J, Arganda-Carreras, I, Frise, E, Kaynig, V, Longair, M, Pietzsch, T, Rueden, C, Saalfeld, S, Schmid, B, Tinevez, JY, White, DJ, Hartenstein, V, Eliceiri, K, Tomancak, P, & Cardona, A (2012). *Fiji: an open-source platform for biological-image analysis.* Nature Methods, Volume 9, Issue 7, pp 676-682.

Thibault, P, Dierolf, M, Bunk, O, Menzel, A, & Pfeiffer, F (2009). *Probe retrieval in ptychographic coherent diffractive imaging*. Ultramicroscopy, Volume 109, Issue 4, pp 338-343.

Thibault, P, & Guizar-Sicairos, M (2012). *Maximum-likelihood refinement for coherent diffractive imaging*. New Journal of Physics, Volume 14, Issue 6, pp 063004.

Thomas, JJ, Jennings, HM, & Allen, AJ (2010). *Relationships between Composition and Density of Tobermorite, Jennite, and Nanoscale CaO−SiO $_{2}$ −H $_{2}$ O*. The Journal of Physical Chemistry C, Volume 114, Issue 17, pp 7594-7601.

Trtik, P, Diaz, A, Guizar-Sicairos, M, Menzel, A, & Bunk, O (2013). *Density mapping of hardened cement paste using ptychographic X-ray computed tomography*. Cement and Concrete Composites, Volume 36, pp 71-77.

Trtik, P, Kaufmann, J, & Volz, U (2012). *On the use of peak-force tapping atomic force microscopy for quantification of the local elastic modulus in hardened cement paste.* Cement and Concrete Research, Volume 42, Issue 1, pp 215-221.

van Heel, M, & Schatz, M (2005). *Fourier shell correlation threshold criteria*. Journal of Structural Biology, Volume 151, Issue 3, pp 250-262.